Dynamic Mode Decomposition of Deformation Fields in Elastic and Elastic-Plastic Solids

C. Hari Manoj Simha

School of Engineering, University of Guelph, 50 Stone Road East, Guelph, ON, Canada N1G 2W1

Abstract

Without recourse to constitutive assumptions, without knowledge of material properties, and without solving any of the conservation equations, we construct deformation fields for linear solids using Dynamic Mode Decomposition (DMD). Originally developed for analyzing experimental or computational field variables in fluid mechanics, it takes as input vectors of flow variables assembled as columns of a data matrix, and requires a remarkably few lines of code. It is a natural fit for solid mechanics wherein surface displacements can be used for the analysis. Vectors of surface displacements are arrayed in columns to created a data matrix. Singular Value Decomposition of the time-shifted data matrix affords selection of dominant modes (rank) in the deformation field. The DMD algorithm operates on time-shifted data matrices, obtains a reduced-order model that can reconstruct the deformation field, and also provides the dominant temporal and spatial modes of the deformation. In the case of linear elastic solids, DMD can be used to: reconstruct or predict the displacement states. In elastic-plastic solids, the transition from elastic to plastic results in the eigenvalues of the low-rank data matrix going out of the unit circle (implying an unstable growth mode). Using a combination of finite element analyses and displacement measurements obtained using Digital Image Correlation (DIC), we make the case for using DMD for state-estimation and state prediction in elastic solids and identifying onset of plasticity in elastic-plastic solids.

Keywords: Data-driven; Dynamic Mode Decomposition; Solid Mechanics; Reduced-Order Model

---

Nomenclature

$\boldsymbol{A}$ Transition matrix to trasfer state k to $k+1$

Preprint submitted to European Journal of Mechanics / A Solids *October 21, 2023*

$\widetilde{\boldsymbol{A}}$	Low rank version $\boldsymbol{A}$
E_r	Euclidean / Frobenius norm
$\boldsymbol{f}$	Vector of functions describing system dynamics
m	Index of snapshot
n	Index of measurement
r	Rank of $\boldsymbol{X}$
t	Time
t, Δt	time and time interval
$\boldsymbol{U}, \boldsymbol{V}$	Unitary matrices from SVD of $\boldsymbol{X}$
$\widetilde{\boldsymbol{U}}, \widetilde{\boldsymbol{V}}$	Low rank versions of $\boldsymbol{U}$, and $\boldsymbol{V}$
$\boldsymbol{W}$	Eigenvectors of $\widetilde{\boldsymbol{A}}$
$\boldsymbol{x}$	State vector
$\boldsymbol{X}, \boldsymbol{X}'$	Time-shifted data matrices
$x\,, y$	x and y coordinates
β	$\beta = m/n$ used in Gavish-Donoho rank truncation
$\boldsymbol{x}_m$	Snapshot of m th measurement
$\boldsymbol{\Lambda}, \lambda$	Eigenvaluesof $\widetilde{\boldsymbol{A}}$
μ	System parameters
τ^*	Gavish-Donoho threshold for rank truncation
$\boldsymbol{\Phi}$	Spatial modes from DMD, size $n \times r$
$\boldsymbol{\Psi}$	Temporal modes from DMD, size $r \times m$

Abbreviations

CFD Computational Fluid Dynamics

DMD Dynamic Mode Decomposition

DIC Digital Image Correlation

POD Proper Orthogonal Decomposition

sg Strain gauge

SVD Singular Value Decomposition

vg Virtual gauge

1. Introduction

Measurements (or results of computations) of field variables such as velocity, temperature, and pressure in fluids can be post-processed using the Dynamic Mode Decomposition (DMD) algorithm to identify spatio-temporal coherent features, and localized instabilities in the flow. Originally developed by Schmid (2010) and Rowley et al. (2009), and applied to flow in channels and jets by Rowley et al. (2009) and Schmid et al. (2011) has received wide attention and within a decade of its introduction, it has found application in thermo-fluids, neuroscience, image-processing, and epidemiological studies; Brunton and Kutz (2019). Monographs by Kutz et al. (2016), Brunton and Kutz (2019), and the recent review by Schmid (2022) provide exposition, extensive bibliography, and algorithms. It is a data-driven method that relies on data obtained through computations, such as Computational Fluid Dynamics (CFD), or Eulerian measurements.

Snapshots of field variables, constitute measurement vectors are obtained at constant (or non-constant) intervals, to obtain data matrix. Singular Value Decomposition (SVD) on the data matrix is carried out and the dominant modes, or rank, of the data are identified. Time-shifted data matrices are obtained and used in the DMD algorithm to obtain a low-rank matrix, *which is a significantly smaller than the larger (original) data matrix and whose eigenvalues and eigenvectors describe the dynamics of the system.* Accordingly, an excessively large data matrix (such as those from CFD) is reduced in size owing to the identification of dominant modes. The DMD algorithm may be interpreted as combining the advantages of the SVD for spatial dimensionality reduction, and Fast Fourier Transform (FFT) for temporal frequency identification; Brunton and Kutz (2019). In this regard, DMD has advantages over Proper Orthogonal Decomposition (POD), which has also been applied on snapshots of data, in that DMD obtains eigenvalues that describe how the mode amplitudes evolve with time; Kutz et al. (2016).

It bears emphasis, that it is a purely data-driven method and does not require: computations of gradients, knowledge of material properties, solution of the conservation equations, underlying physics (constitutive assumptions), or knowledge of the system boundary conditions.

For linear systems, the DMD algorithm obtains the leading eigenvalues and eigenvectors; and for periodic data, the decomposition is equivalent to a discrete Fourier transform; Rowley et al. (2009). In passing, we note that DMD can be implemented in a few lines of code; see, for instance, page 240 of Brunton and Kutz (2019).

The DMD algorithm has been applied to systems that are linear, systems that also display periodic responses, and quasi-periodic responses in non-linear systems; Kutz (2013). The DMD operator can be connected to the Koopman operator as discussed by Rowley et al. (2009).

Despite its popularity, DMD has not found wide use in solid mechanics. It is a natural fit to the discipline as displacement fields, from surfaces of solids, which are routinely measured using Digital Image Correlation (DIC) or image-processing methods, can be used to setup a data matrix. Saito and Kuno (2020) obtained damping coefficient and natural frequencies of a vibrating cantilever using DMD. Das et al. (2020) used finite element computations, and obtained snapshots of displacements and velocities to model the deformation of a pneumatically activated soft-robotic finger. Simha and Biglarbegian (2022), used snapshots from finite element computations, and pointed out its power in developing reduced order models, and predicting states for elastic and non-linear elastic materials. DMD models may fail to generalize beyond the training data, or are susceptible to noise in the data, and to overcome these, Baddoo et al. (2023) developed physics-informed DMD. They discuss self-adjoint operators that are pervasive in mechanics.

In this paper, we further develop the application of the DMD to elastic, and elastic-plastic solids. Data in this work are not noisy and we assume that the underlying physics and physical properties are unknown. Section 3 presents background on the algorithm, and the un-supervised rank truncation approach advocated in this work. We use two-dimensional, finite element analyses to make the case for applying DMD to surface displacement fields of elastic and elastic-plastic solids; see Section 4. To support the theoretical analysis, DIC measurements of displacement fields are used for DMD analyses, in Section 5. Finally, we conclude with a Summary and Discussion in Section 6.

2. Notation

Boldface is used to denote vectors and matrices; $\boldsymbol{I}$ is the identity matrix, $\dagger$ is the Moore-Penrose inverse, $*$ is the complex, conjugate transpose , superscript -1 is the inverse of a square matrix. Variable names and conventions are similar to the treatment in Brunton and Kutz (2019). An overtilde is used to denote matrices that are low-rank; those without the overtilde are full-rank. Frobenius (or Euclidean) norm for matrix $\boldsymbol{X}$ is denoted by $||\boldsymbol{X}||_2$.

3. Background on DMD

A brief outline of DMD is presented here; general details may be found in Brunton and Kutz (2019) and also details specific to mechanics in Simha and Biglarbegian (2022). Partial differential equations, upon suitable discretization can be reduced to a vector of dynamical equations as

$$\frac{d\boldsymbol{x}}{dt} = \boldsymbol{f}(\boldsymbol{x}, t; \mu)\,,$$

where $\boldsymbol{x}$ is a state vector, t is time, $\boldsymbol{f}$ denotes the dynamics, and μ are system parameters. The DMD algorithm assumes local linearity and replaces the above with

$$\frac{d\boldsymbol{x}}{dt} = \mathcal{A}\boldsymbol{x}\,, \tag{1}$$

which has the solution $\boldsymbol{x}(t) = \boldsymbol{x}(0)\exp(\boldsymbol{\mathcal{A}}t)$, where $\boldsymbol{x}(0)$ is the initial condition. Dynamic Mode Decomposition solves Eq. (1) by obtaining the snapshots of $\boldsymbol{f}()$, each of which is a column vector of size $n \times 1$ and there are $m+1$ measurements, which obtains matrices $\boldsymbol{X}$ and $\boldsymbol{X}'$ as

$$\boldsymbol{X} = \begin{bmatrix} | & | & | & | \\ \boldsymbol{x}_1 & \boldsymbol{x}_2 & \cdots & \boldsymbol{x}_m \\ | & | & | & | \end{bmatrix}$$

$$\boldsymbol{X}' = \begin{bmatrix} | & | & | & & | \\ \boldsymbol{x}_2 & \boldsymbol{x}_3 & \cdots & & \boldsymbol{x}_{m+1} \\ | & | & | & & | \end{bmatrix}, \tag{2}$$

where the vertical lines in the matrix indicate that each vector is a stack of measurements, and each of the vectors represents a state at a given time. Here, we assume that the snapshots are sampled at constant intervals Δt ; non-constant sampling of the snapshots is also possible; see Tu et al. (2014). In the case of fluids, the vectors comprise velocities/temperatures/pressure from flow fields; in the case of solids, surface displacements are a natural fit. At its essence, DMD obtains a best-fit operator $\boldsymbol{A}$ that advances the initial state to the next through

$$\boldsymbol{X}' = \boldsymbol{A}\boldsymbol{X}\,, \tag{3}$$

where $\boldsymbol{A}$ can be interpreted as a least-squares/minimum-norm solution to $\boldsymbol{X}' = \boldsymbol{A}\boldsymbol{X}$. Using the Moore-Penrose inverse, denoted by $\dagger$, leads to

$$\boldsymbol{A} = \boldsymbol{X}'\boldsymbol{X}^{\dagger}\,. \tag{4}$$

For connections of $\boldsymbol{A}$ with the Koopman operator, see Brunton and Kutz (2019). Operator $\boldsymbol{A}$ can be used to transition from state to state as

$$\boldsymbol{x}_{k+1} \approx \boldsymbol{A}\boldsymbol{x}_k\,. \tag{5}$$

Matrix $\boldsymbol{A}$ is constructed so that the Euclidean norm $||\boldsymbol{x}_{k+1} - \boldsymbol{A}\boldsymbol{x}_k||_2$ is minimized across all of the snapshots; Rowley et al. (2009). Equation (5) is the discrete version of Eq. (1) sampled with Δt and $\boldsymbol{A} = \exp(\mathcal{A}\Delta t)$. Using Eq. (5), noting that $\boldsymbol{A}$ can be used in a recursive fashion, with a knowledge of the initial state $\boldsymbol{x}_1$, terminal state $\boldsymbol{x}_m$ is predicted using

$$\boldsymbol{X} \approx \begin{bmatrix} | & | & | & & | \\ \boldsymbol{x}_1 & \boldsymbol{A}\boldsymbol{x}_1 & \cdots & & \boldsymbol{A}^{m-1}\boldsymbol{x}_1 \\ | & | & | & & | \end{bmatrix}. \tag{6}$$

The first step in the DMD algorithm is to compute an SVD of $\boldsymbol{X}$ as

$$\boldsymbol{X} \approx \widetilde{\boldsymbol{U}}\widetilde{\boldsymbol{\Sigma}}\widetilde{\boldsymbol{V}}^*, \tag{7}$$

where $\widetilde{\boldsymbol{U}} \in \mathbb{C}^{n\times r}$, $\widetilde{\boldsymbol{\Sigma}} \in \mathbb{C}^{r\times r}$, and $\widetilde{\boldsymbol{V}} \in \mathbb{C}^{m\times r}$, $r \le m$ is the either the exact or approximate rank of the data matrix $\boldsymbol{X}$. Here, $*$ denotes the complex conjugate transpose. Columns of $\widetilde{\boldsymbol{U}}$ are the proper orthogonal modes of $\boldsymbol{X}$ and satisfy $\widetilde{\boldsymbol{U}}\widetilde{\boldsymbol{U}}^* = \widetilde{\boldsymbol{U}}^*\widetilde{\boldsymbol{U}} = \boldsymbol{I}$. Likewise, $\widetilde{\boldsymbol{V}}\widetilde{\boldsymbol{V}}^* = \widetilde{V}^*\widetilde{\boldsymbol{V}} = \boldsymbol{I}$. The r modes can be chosen by identifying those deemed to have sufficient magnitude to contribute to the dynamics; or they can be selected in an un-supervised manner as discussed next.

Taking the Moore-Penrose inverse of Eq. (7) yields $\boldsymbol{X}^\dagger = \widetilde{\boldsymbol{V}}\widetilde{\boldsymbol{\Sigma}}^{-1}\widetilde{\boldsymbol{U}}^8$, substituting in Eq. (4) gives

$$\boldsymbol{A} = \boldsymbol{X}'\widetilde{\boldsymbol{V}}\widetilde{\boldsymbol{\Sigma}}^{-1}\widetilde{\boldsymbol{U}}^*. \tag{8}$$

Similarity transformation is used to project $\boldsymbol{A}$ onto the r POD modes (Schmid (2010)) yields a lower dimensional matrix of size $r \times r$ as

$$\widetilde{\boldsymbol{A}} = \widetilde{\boldsymbol{U}}^*\boldsymbol{A}\widetilde{\boldsymbol{U}} = \widetilde{\boldsymbol{U}}^*\boldsymbol{X}'\widetilde{V}\widetilde{\boldsymbol{\Sigma}}^{-1}. \tag{9}$$

Matrix $\widetilde{\boldsymbol{U}}$, can be used to reconstruct the full state $\boldsymbol{x}_k$, Brunton and Kutz (2019) or Chapter 13 of Smith (2013).

Here we note that the full state $\boldsymbol{x}$ can be reconstructed using the low-rank state and $\widetilde{\boldsymbol{U}}$ as

$$\boldsymbol{x}_k = \widetilde{\boldsymbol{U}}\widetilde{\boldsymbol{x}}_k. \tag{10}$$

Eigenvectors and eigenvalues of $\widetilde{\boldsymbol{A}}$ can be obtained through

$$\widetilde{\boldsymbol{A}}\boldsymbol{W} = \boldsymbol{W}\boldsymbol{\Lambda}\,, \tag{11}$$

where $\boldsymbol{W}$ and $\boldsymbol{\Lambda}$ (both size $r \times r$) are the eigenvectors and eigenvalues of $\widetilde{\boldsymbol{A}}$, respectively. Schmid (2010) computes the eigenvectors of the high-dimensional system using $\boldsymbol{\Phi} = \widetilde{\boldsymbol{U}}\boldsymbol{W}$; alternatively, Tu et al. (2014) proposed the following projection of size $n \times r$ as

$$\boldsymbol{\Phi} = \boldsymbol{X}'\widetilde{\boldsymbol{V}}\widetilde{\boldsymbol{\Sigma}}^{-1}\boldsymbol{W}. \tag{12}$$

and derived the remarkable result that $\boldsymbol{A}\boldsymbol{\Phi} = \boldsymbol{\Phi}\boldsymbol{\Lambda}$, which shows that the modes constructed using the reduced matrices are identical to the modes of the high-dimensional matrix.

Noting that Eq. (9) implies $\boldsymbol{A} = \widetilde{\boldsymbol{U}}\widetilde{\boldsymbol{A}}\widetilde{\boldsymbol{U}}^*$, substituting in Eq. (5) and using the properties of $\boldsymbol{U}$ yields

$$\boldsymbol{x}_{k+1} = \widetilde{\boldsymbol{U}}\widetilde{\boldsymbol{A}}\widetilde{\boldsymbol{U}}^*\boldsymbol{x}_k\,, \text{and}$$
$$\boldsymbol{x}_{k+2} = \widetilde{\boldsymbol{U}}\widetilde{\boldsymbol{A}}\widetilde{\boldsymbol{U}}^*\boldsymbol{x}_{k+1} = \widetilde{\boldsymbol{U}}\widetilde{\boldsymbol{A}}^2\widetilde{\boldsymbol{U}}^*\boldsymbol{x}_k\,.$$

The above suggests the following recursive reconstruction using the low-rank matrices as

$$\boldsymbol{x}_m^{DMD} = \begin{bmatrix} | & | & | & | & | \\ \boldsymbol{x}_1 & \widetilde{\boldsymbol{U}}\widetilde{\boldsymbol{A}}\widetilde{\boldsymbol{U}}^*\boldsymbol{x}_1 & \widetilde{\boldsymbol{U}}\widetilde{\boldsymbol{A}}^2\widetilde{\boldsymbol{U}}^*\boldsymbol{x}_1 & \cdots & \widetilde{\boldsymbol{U}}\widetilde{\boldsymbol{A}}^{m-1}\widetilde{\boldsymbol{U}}^*\boldsymbol{x}_1 \\ | & | & | & | & | \end{bmatrix}. \tag{13}$$

Another method of reconstruction uses the eigenvalues and eigenvectors of $\widetilde{\boldsymbol{A}}$ and further details may be found in Brunton and Kutz (2019). Listing of the DMD pseudo-code is in Algorithm 1.

3.1. Rank Truncation

Rank r can be obtained by plotting the singular values of $\boldsymbol{X}$, and choosing dominant values that are deemed to contribute to the response. Alternatively, a hard threshold proposed by Gavish and Donoho (2014) allows for unsupervised selection of the rank of $\boldsymbol{X}$ based on its singular values. The selection being valid when matrix size is large compared with the rank, and the signal-to-noise ratio of the low-rank matrix stays constant. Gavish-Donoho propose the following algorithm:

$$\tau^* = f(\beta)\, median(diag(\boldsymbol{\Sigma})),$$

where $\beta = m/n$ is the ratio of number of snapshots to number of measurements, *diag* stands for diagonal matrix, and *median* is the statistical measure. If the signal-to-noise ratio is known, an analytical formula for $f(\beta)$ is given by Gavish and Donoho (2014); alternatively, they give an approximate function as

$$f(\beta) \approx 0.56\beta^3 - 0.95\beta^2 + 1.82\beta + 1.43.$$

Rank of $\boldsymbol{X}$ corresponds to the element of $diag(\boldsymbol{\Sigma})$ that is closes to τ^*.

Algorithm 1 DMD algorithm; adapted from Kutz et al. (2016).

1. Set up time-shifted matrices $\boldsymbol{X}$ and $\boldsymbol{X'}$.
2. Carry out SVD on $\boldsymbol{X} = \boldsymbol{U\Sigma V^*}$, and choose the rank r for truncation.
3. Obtain $\widetilde{\boldsymbol{U}}$, $\widetilde{\boldsymbol{V}}$ and $\widetilde{\boldsymbol{\Sigma}}$ using r, $\boldsymbol{U}$, $\boldsymbol{V}$, and $\boldsymbol{\Sigma}$.
4. Compute $\widetilde{\boldsymbol{A}} = \widetilde{\boldsymbol{U}}\boldsymbol{\Sigma}\widetilde{\boldsymbol{V}}^*$.
5. Compute eigenvectors $\boldsymbol{W}$ and eigenvalues $\boldsymbol{\Lambda}$ of $\widetilde{\boldsymbol{A}}$.

4. DMD on Computational Data

We use the Abaqus finite element software to obtain snapshots of surface displacements obtained from two-dimensional (2D) computations carried out in the $x - y$ plane, and apply the DMD algorithm on them. When the implicit solver is used to solve static problems, time is a fictitious parameter and serves as a fiducial for the loading. Python scripts were used to output nodal coordinates (x, y) and displacements (u, v) in 2D at constant intervals, and these serve as inputs to the DMD algorithm.

4.1. Elastic Computations

Consider first, the elastic case; a quarter finite element model of a plate with a hole is shown in Fig. 1; x and y symmetries were applied on the $y = 0$ and $x = 0$ lines, respectively; and displacement-controlled loading was applied on the right-hand edge of the plate. Constant strain, plane-stress triangular elements (CPS3) were used for the mesh. Material was taken to be steel with density, Young's modulus, and Poisson's ratio of 7800 kg/m^3, 200 GPa, and 0.33, respectively.

A displacement of 0.05 mm was applied as a ramp over a period of 0.5 s. Here, time in seconds is an arbitrary unit. Snapshots of displacements (u, v) for every 0.01 seconds were obtained; that is, a total of $m = 50$. The mesh had a total of 1844 nodes. It follows then that, the entire displacement field can be represented by 3688×50 numbers. Size of the snapshots and time-shifted data matrices are:

$$\boldsymbol{x}_i \text{ is } 3688 \times 1$$
$$\boldsymbol{X} \text{ is } 3688 \times 49$$
$$\boldsymbol{X'} \text{ is } 3688 \times 49.$$

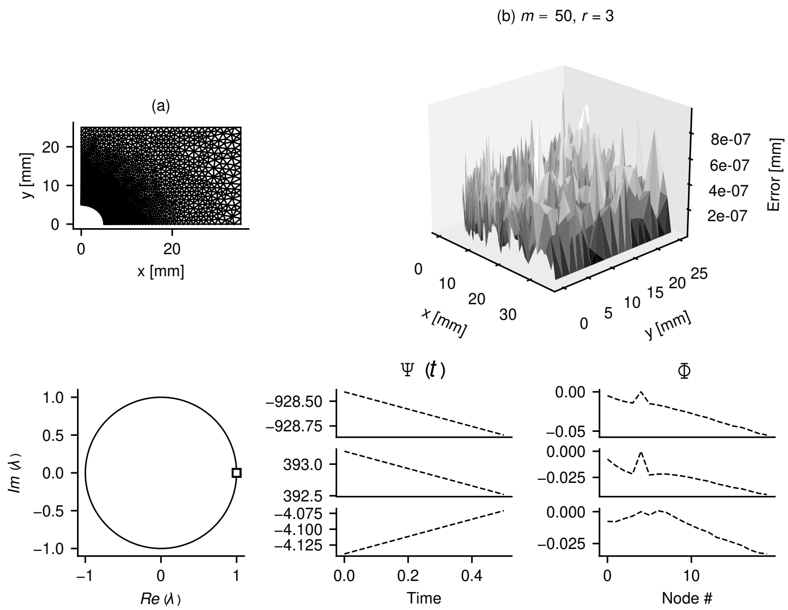

Figure 1: Reconstruction of elastic deformation field. (a) Quarter-model mesh. (b) Surface plot of error in mm, with all of the snapshots included. Bottom: Unit circle with eigenvalues of $\widetilde{\boldsymbol{A}}$, plots of $\boldsymbol{\Psi}$ and $\boldsymbol{\Phi}$.

We perform DMD using $\boldsymbol{X}$and $\boldsymbol{X'}$ and obtain rank r, $\widetilde{\boldsymbol{U}}$, $\widetilde{\boldsymbol{A}}$; the initial state $\boldsymbol{x_i}$ is known by definition. We can obtain the displacement state of the plate for snapshot m using the sequence in Eq. (13) and compare with the known $\boldsymbol{x}_m$ using the Frobenius norm

$$E_r = \left|\left|\boldsymbol{x}_m - \boldsymbol{x}_m^{DMD}\right|\right|_2 . \tag{14}$$

We start with a data matrix of size $n \times m$, and we attempt to reconstruct the final state with only $\widetilde{\boldsymbol{U}}$, $\widetilde{\boldsymbol{A}}$. That is data of size $n \times r \, + \, r \times r$.

Figure 1 presents the prediction error for each of the nodes in the final state, $m = 50$ and a rank $r = 3$. Here, with a knowledge of the initial vector $\boldsymbol{x}_1$ and $3688 \times 3 + 3 \times 3$ pieces of data, we can reconstruct the deformation field, which is $\sim 6\%$ of all of the data.

The figure also shows the eigenvalues of the $\widetilde{\boldsymbol{A}}$ matrix and all of them are approximately unity and lie on the perimeter of the unit circles; vectors $\boldsymbol{\Phi}$ and $\boldsymbol{\Psi}$ are also plotted. In particular, $\boldsymbol{\Phi}$ represents spatial structures, and only the first twenty items (out of 3688) are shown and these represent x displacements. Node number 20 is on the $y-$symmetry plane on the right edge of the plate. To understand what these vectors represent, consider the sum over the three modes

$$\mathbf{\Phi}(20,0)\mathbf{\Psi}(0.5,0) + \mathbf{\Phi}(20,1)\mathbf{\Psi}(0.5,1) + \mathbf{\Phi}(20,2)\mathbf{\Psi}(0.5,2) = 35.0499998\,,$$

where the first number in the parenthesis of $\mathbf{\Phi}$ is node number, and the second number is the mode number; the first number parenthesis of $\mathbf{\Psi}$ is time and the second is the mode number. Note that node 20 is on the x axis and the right edge of the the plate.The above sum differs from the expected $x-$displacement of 35.05 mm by order of 10^{-7}mm. Also note that $\mathbf{\Phi}$ display a spike with value of 0, these correspond to the nodes on the $x-$symmetry plane, which are restrained.

Alternatively, we use only few snapshots to *predict* the final state, and the reconstruction error depends on the number of snapshots. For instance, in Fig. 2(a), when $m = 20$, $r = 8$ reconstruction yields error an order of magnitude higher than the reconstruction using all of the snapshots. Using only 15 snapshots and $r = 5$ yields errors of the order of 10^{-5}mm.

Rank truncation using the Gavish and Donoho (2014) method yields 5 modes in this instance, and as shown in the plot of the eigenvalues of the $\tilde{\boldsymbol{A}}$ matrix, can also be obtained by selecting the mode after which there is no significant change in the value of the eigenvalue. Figure 2 (e) shows the unit circle and the location of the eigenvalues. As with the case with $m = 49$, where we used all of the snapshots, the three dominant eigenvalues are unity and on the unit circle, however there are additional complex eigenvalues, which when matched with the time-dependent amplitudes, which are initially oscillatory (of the order of 10^{-7}mm) and decay to zero, do not contribute to the final displacements.

4.2. Elastic-Plastic Computations

We assumed that the plate studied in the previous section is an elastic-plastic material and apply DMD to the computed displacements. In addition to the properties previously listed, yield strength was taken to be 100 MPa. In this instance, we apply the DMD algorithm in an on-line sense. That is, acquire a snapshot, augment the $\boldsymbol{X}$ and $\boldsymbol{X'}$ matrices and assess the resultant modes and eigenvalues. Articles by Hemati et al. (2014); Nayak et al. (2023); Alfatlawi et al. (2020); Barros et al. (2023) discuss other strategies and considerations

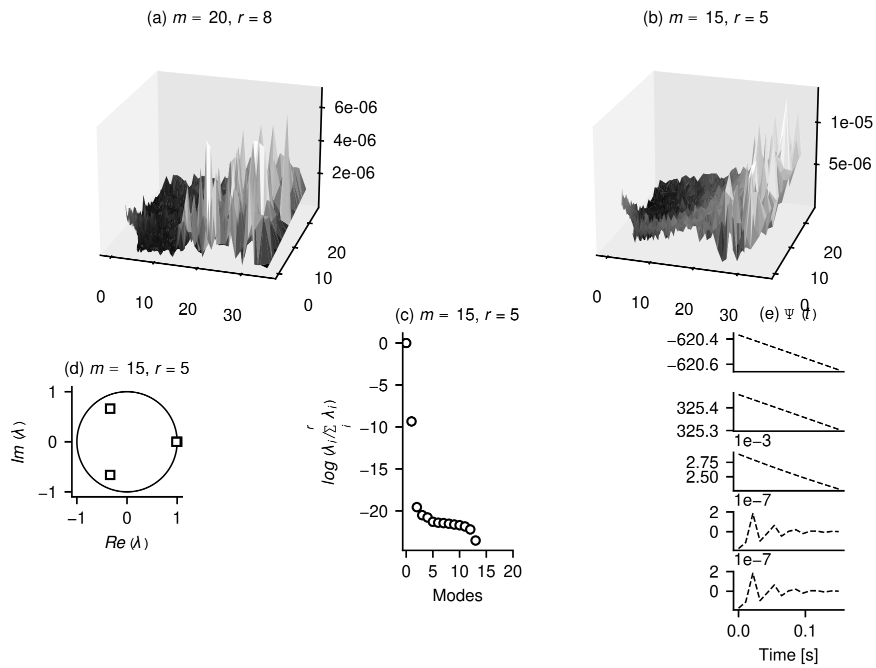

Figure 2: (a) and (b) reconstruction of elastic deformation field with fewer snapshots. (c) Plot of normalized eigenvalues of the $\tilde{\boldsymbol{A}}$ matrix before truncation. (d) All eigenvalues are in the unit matrix. (e) Plots of the temporal modes.The first three are dominant and the last two die out to zero.

when applying DMD for data that is acquired sequentially rather than as a batch.

Figure 3 (a) shows the *global* load-displacement curve and the first dotted vertical line indicates that global response is elastic for snapshot $m = 8$, and the second vertical line for $m = 12$ indicates that the global response is plastic. Compare the linearity of the load-displacement curve with the dashed line, plotted in the figure as a reference.

Error plots in Fig. 3 tell a different story. The reconstruction error for state $m = 7$ is of the order of 10^{-6} mm, which suggests, based on the reconstruction errors in the previous section, that the local response is elastic. For state $m = 8$, the reconstruction error blows up to the order of 100 mm, which suggests that the DMD algorithm has broken down, and presumably this is is owing to local plasticity, which is in contrast to the observation in the load-displacement curve that indicates global linearity for $m = 8$. Even if we double the number of retained modes to $r = 6$, the error is not impacted.

This is a key result and indicates the global load-displacement curve displays the onset of non-linear behavior in the structure, when it ceases to be a straight line; the DMD algorithm, on the other hand, identifies the onset of **local plasticity, especially at the north pole of the hole.** We make further case for this in the next figure.

With the acquisition of more snapshots, the reconstruction error improves to approximately 10^{-3} mm and is shown in Figure 3 (b) for a state $m = 15$. As plasticity spreads in the plate with further increase of global displacement, the gradients in displacement are informed by the additionally acquired snapshots. However, owing to the non-linear material response, the reconstruction error does not go below the value of 10^{-3} mm.

The Abaqus post-processor outputs a binary (0 or 1) field variable called yield flag whose level indicates whether the von-Mises stress has exceeded the yield strength of the material. Figure 4 (a) presents a close up view of the perimeter of the hole in the plate and superimposed is the contours of the yield flag for $m = 7$ there is incipient yield and because of nodal averaging, the value of the flag is below unity around the perimeter of the hole. Subsequently, when $m = 8$, contours of the yield flag around the north-pole of the hole shown in Fig. 4 (b) indicates plasticity around the north-pole of the hole and it corroborates the result obtained using the DMD algorithm.

The more striking result is in Fig. 4 (c) wherein the eigenvalue of the the $\tilde{\boldsymbol{A}}$ matrix (size $r \times r$) is outside the unit circle, in the right side of the imaginary

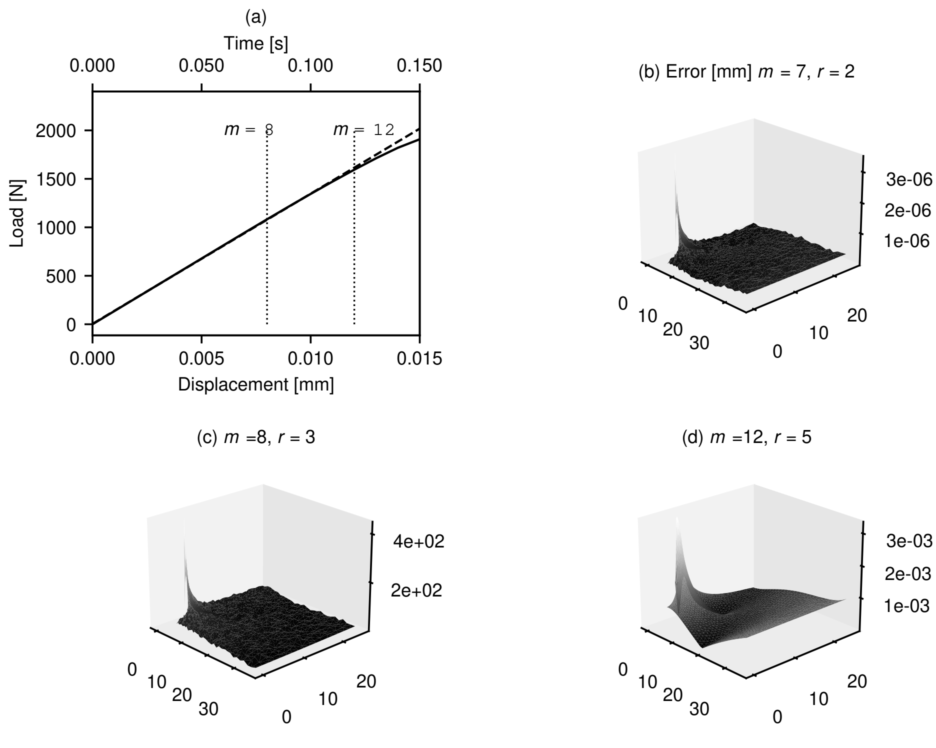

Figure 3: (a) Global load-displacement plot. Vertical lines correspond to elastic behavior for $m = 8$, and onset of global plastic response for $m = 12$. Dashed line shows departure from linearity in the force-displacement curve. (b) Error surface plot prior to onset of local plasticity for $m = 7$. (c) Error surface plot after onset of local plasticity - corresponds to first vertical dashed line in panel, $m = 8$. (a). (d) Error surface plot at 0.012 mm of global displacement; $m = 12$.

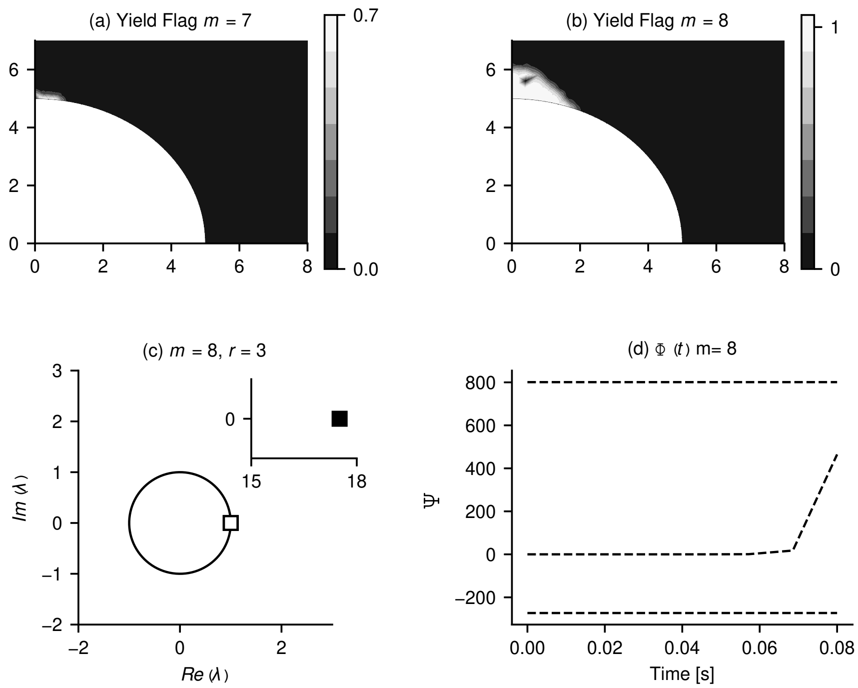

Figure 4: (a) Zoomed in contour plot of yield flag for state $m = 7$; no significant plasticity yet. (b) Contour plot of yield flag from $m = 8$; significant plasticity around the north pole of the hole. (d) Unit circle showing the three eigenvalues. Two are close to unity on the real axis. The third is out of the unit circle (at approximately 17.5) and shown as a filled in square in the inset. (d) Plot of modes, showing the dominant mode displaying a significant increase in magnitude with the onset of plasticity.

plane, indicating instability in the sense of classical control theory. Corresponding mode shows a dramatic rise with time; Fig. 4 (d). In what follows, we use Digital Image Correlation on elastic-plastic solids to assess whether the latter result can be reproduced when DMD is applied to experimental measurements.

5. DMD on Experimental Data

5.1. Materials and Methods

Standard ASTM E8 tensile specimens of cold-rolled 1018 steel and aluminum Al6061 plates with a hole in them were axially loaded in a 50-kN Instron frame. The tensile specimen was 18.36-mm wide, 3.2-mm thick, and had a gauge section of 50 mm. The Aluminum plate was 25-mm wide, 3-mm thick, 200-mm long, and had a hole in the center of 5-mm radius. For both of the specimen geometries, three tests were conducted to ensure repeatability. It bears emphasis that knowledge of the material properties and specimen geometries are not required for the DMD algorithm.

Figure 5 presents photos of the experimental setup for the two-dimensional DIC. Speckle patterns were applied by spraying black and white paint on one side and a CEA-06-125UN-350 Micro Measurements resistance strain gauge was bonded to the other side of the specimen. In the tensile specimen, the gauge was bonded in the gauge section, and in the structure with the hole, the gauge was bonded in the region where the deformation would be elastic.

A standard Digital Single Lens Reflex camera (Canon, EOS Rebel T7 with 24-megapixel sensor) in conjunction with a Sigma 18-300 mm F33.5-6.3 Macro lens was used to record video of the deformation of the specimen's surface. Start of the loading and video recording were synchronized and video was captured a framing rate of 30 frames per second. The strain gauge was bonded using standard procedure, and is used with a Tacuna Systems (EMBSGB200) load-cell amplifier to measure strain.

The video was recorded as an mp4 file and images were sampled with a fixed frequency (skipping 2 frames). These images were then input to a Digital Image Correlation engine (DICe) developed by Turner (2015). The latter is an open-source DIC analysis software. We used it in two modes; first by specifying a window and tracking subsets of the order of 15 pixels. This resulted in coordinates of approximately 1400 points being tracked. That is, 1400 displacements (u, v) pairs per snapshot. As we know the number of frames skipped in the video file and the framing rate, the time stamp of each snap shot can be obtained.

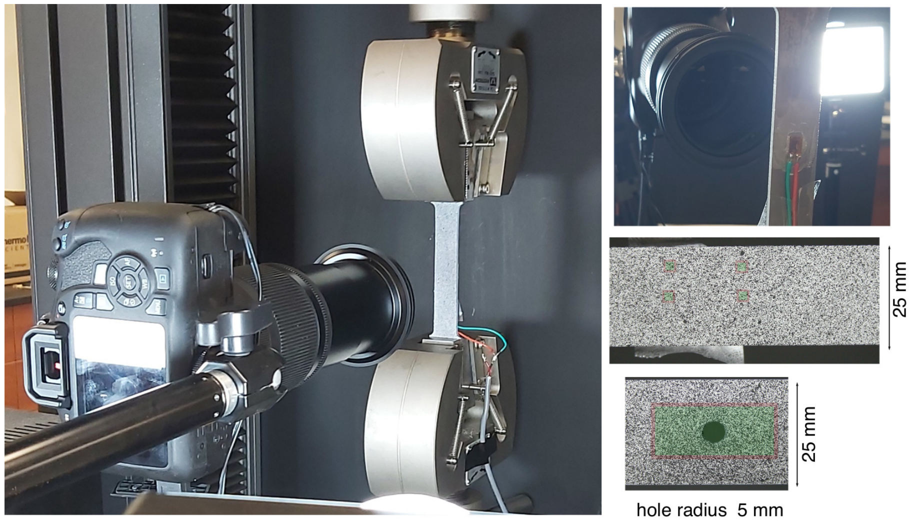

Figure 5: Photos of the experimental setup. Left: DIC side of dog-bone specimen in grips of tensile frame. Right top: strain gauge installed opposite to the DIC side of the specimen. Bottom: Regions of Interest used in the plate-with-hole aluminum 6061-specimen, and window used in analysis of tensile 1018-steel specimen.

Alternatively, we specified pairs of regions of interest each of the order of 20 pixels and used the average coordinates of the center to compute true strains. We compare the latter strains with the strain measurement from the bonded resistance strain gauge to validate our DIC setup.

5.2. DMD on Tensile Specimen

We first address the results of the analysis on the tensile specimens; see Fig. 6. Graphs in the top row show the results of the strain history (in the gauge section of the specimen) from the bonded resistance strain gauge and virtual strain gauges. Good agreement between the resistance gauge and the virtual gauges from DIC, validates our optical and post-processing workflow. Three vertical dotted lines are shown at approximately 18, 21 and 31 s, respectively.

Axial load history is also shown in the graph through a second $y-$axis. A dotted reference line is also shown, which identifies the **onset of global non-linearity**.

The first dotted vertical line at 18 s is in the elastic portion of the global response, the second vertical line at 21 s is at the start of global non-linear response, and the third vertical line at 31 s is when the load is almost constant.

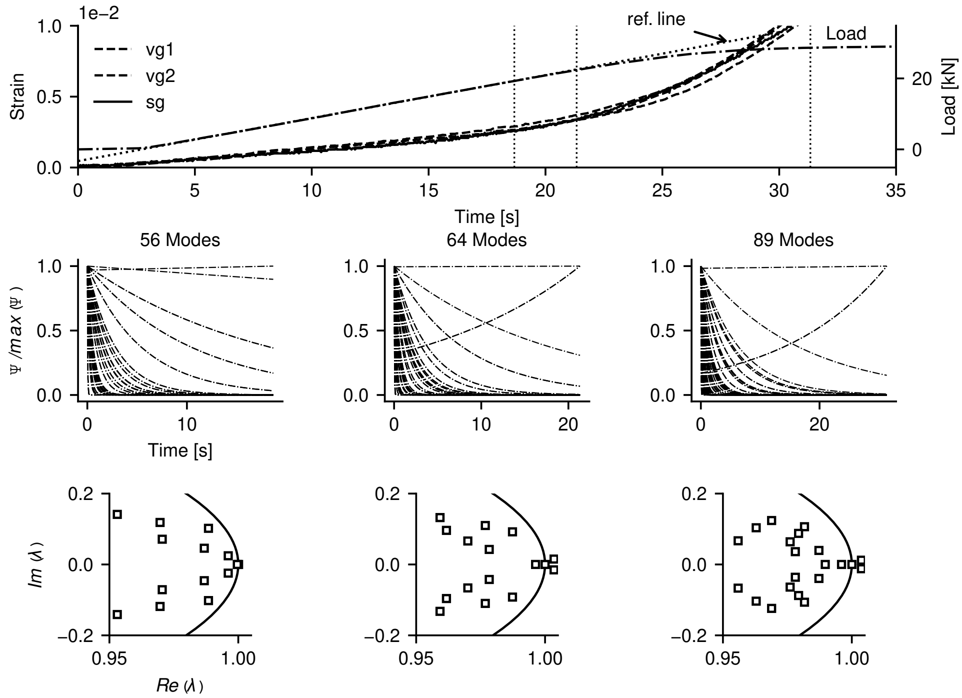

Figure 6: **Top:** Strain histories from bonded resistance strain gauge and DIC; load history on second vertical axis. Reference line indicates onset of non-linearity in the load-displacement curve. Three vertical dotted lines indicate times for which the modes and unit circles are plotted below. **Middle:** Normalized r modes for the three times. For elastic response, the modes are decaying; when plasticity starts, three of the modes rise dramatically. **Bottom:** Unit circles and eigenvalues for the three times. When response is elastic all of the eigenvalues are in the unit circle. With onset of plasticity, the eigenvalues fall out of the circle.

Second and third row of graphs in the figure display the modes and eigenvalues for the three timestamps, respectively. At 18 s, the Gavish-Donoho rank truncation yields 56 modes and all of the modes are decaying as shown.

At 21 s, 64 modes are retained, and there are three eigenvalues out of the unit circle, and this corresponds to the three modes that rise dramatically. Likewise when there is significant plastic strain (at 31 s) in the structure, the eigenvalues are still outside the unit circle with corresponding rising modes.

The key result of the figure, is that the onset of global and local plasticity coincide owing to uniform deformation in the gauge section, and the DMD algorithm unambiguously identifies this with both rising modes and location of the eigenvalues outside the unit circle.

5.3. DMD on plate with hole

Next we consider application of DMD on a structure with a flaw. Figure 7 presents strain histories at the top; and the strains are from the virtual gauges, and the bonded strain gauge. Owing to the localization of plasticity within the structure, strain values plateaus and does not grow further. In the top graph, there are three vertical lines at 14.8, 22, and 36 s, respectively. Comparison of the strain histories obtained using virtual gauges and the resistance gauge validates our DIC workflow.

The graph at the top also shows the load history, and a dotted reference line identifies the point of **non-linearity in structural response**, which occurs around 31 s. The first and second vertical lines are at 14.8 and 22 s, respectively and located in the elastic portion of the global structural response; in contrast, the strain histories indicate that the local response is elastic at 14.8 s and plasticity has started at 22 s (owing to the curvature in the strain-history curve).

The second and third rows of graphs are the DMD modes and eigenvalues with unit circle. All of the modes in the elastic region (at 14.8 s) decay and the eigenvalues are in the unit circle. In contrast, there is a growing mode at 22 s, and one of the eigenvalues is out of the unit circle. Subsequently at 36 s, three modes are increasing rapidly, with three eigenvalues out of the unit-circle.

The key result here is that the DMD algorithm identifies the onset of local plasticity, while the global structural response is elastic.

6. Discussion and Summary

At the outset, we classified uses of DMD into the three categories of state estimation and future-state prediction, identification of features in experimental measurements, and control. It is well known that standard DMD cannot characterize non-linear phenomena; see sec. 7.2 of Brunton and Kutz (2019). However, as shown in this work, for linear elastic systems, DMD can be used to reconstruct the deformation fields to very high accuracies of the order of 10^{-7} mm, and can serve as a reduced order model. Furthermore, for control of linear structures, the DMD algorithm provides means of constructing accurate models.

We have also made the case for the capacity of DMD algorithm for future-state prediction in linear elastic solids. We have shown that the breakdown of DMD in linear systems can be used to identify onset of global and local plasticity.

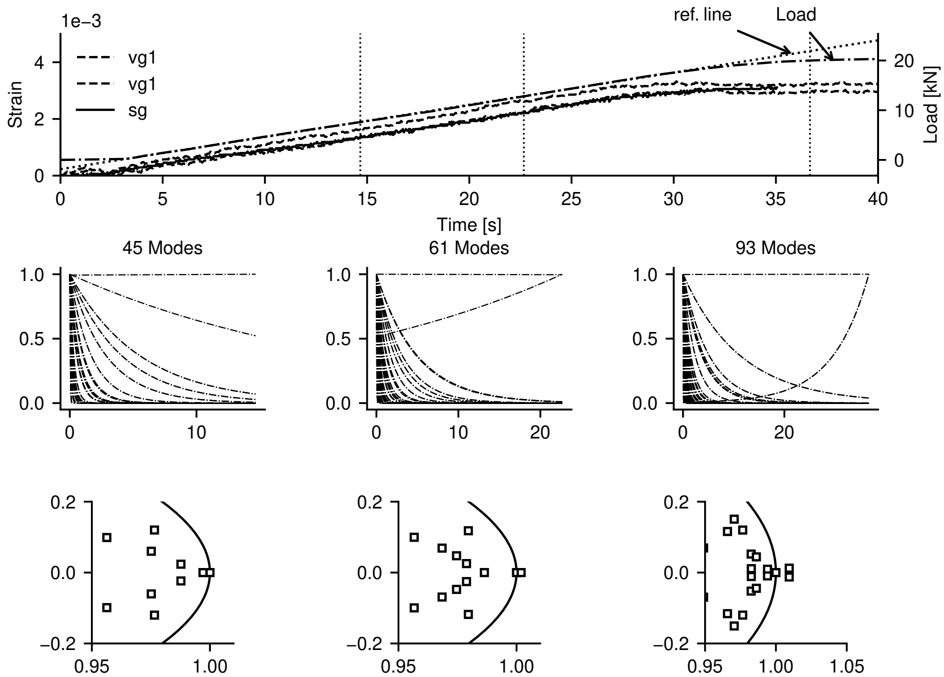

Figure 7: **Top:** Strain histories from bonded resistance strain gauge and DIC; load history on second vertical axis. Reference line indicates onset of non-linearity in the load-displacement curve. Three vertical dotted lines indicate times for which the modes and unit circles are plotted below. **Middle:** Normalized r modes for the three times. For elastic response, the modes are decaying; when plasticity starts, three of the modes rise dramatically. **Bottom:** Unit circles and eigenvalues for the three times. When response is elastic all eigenvalues are in the unit circle. With onset of plasticity, the eigenvalues fall out of the circle.

For instance, in the plate-with-hole structure, we could select a window for DIC analysis that is around the hole (as shown in Fig. 5), a second window in the elastic region, and the DMD analysis would accordingly indicate onset of plasticity in the former, and elasticity in the latter.

Our result that DMD picks out onset of local plasticity in an unsupervised fashion points to to a new technique for the assessment of structural integrity of structures. Accordingly, there is potential for application on three-dimensional displacement data obtained using Digital Volume Correlation (using tomography). Both surface and volume data used in conjunction with DMD has potential to detect onset of structural failure and damage.

Limitations of the DMD technique are in regards to responses of transient dynamics, and rotational and translation invariance; Kutz et al. (2016). Modifications to the basic DMD algorithm to over come these limitations have been developed; Brunton and Kutz (2019). Rowley et al. (2009) have developed DMD algorithm for non-linear flows using Koopman theory, and it presents significant potential for describing the dynamics of non-linear systems; see also Brunton and Kutz (2019).

Nayak et al. (2023)Alfatlawi et al. (2020)

The highlights of the purely data-driven DMD algorithm applied in this work dePeng et al. (2022)serve emphasis:

1. No knowledge of the material properties is required.
2. No knowledge of the boundary conditions are required; as we applied the DMD algorithm to a window, only the state of displacement in the window was required.
3. We did not evaluate gradients to compute strains.
4. No analytical or numerical solution of the conservation equations is required.
5. The basic DMD, as presented in this work, can be implemented with a few lines of code (see sec. 7.2 of Brunton and Kutz (2019)).

Upon publication of the paper, the codes and data will be available at `https://github.com/csimha/DMD_solid_R0`.

7. Acknowledgments

Funding from the Natural Sciences and Engineering Research Council of Canada through the Discovery Grant is gratefully acknowledged. The assistance of graduate student Randall Vandyk in carrying out the experiments is much appreciated.

References

Mustaffa Alfatlawi, Vaibhav Srivastava, and ,Electrical and Computer Engineering Department, Michigan State University, East Lansing, MI 48824, USA. An incremental approach to online dynamic mode decomposition for time-varying systems with applications to EEG data modeling. *Journal of Computational Dynamics*, 7(2):209–241, 2020.

Peter J. Baddoo, Benjamin Herrmann, Beverley J. McKeon, J. Nathan Kutz, and Steven L. Brunton. Physics-informed dynamic mode decomposition. *Proceedings of the Royal Society A: Mathematical, Physical and Engineering Sciences*, 479(2271):20220576, March 2023.

Gabriel F. Barros, Malú Grave, José J. Camata, and Alvaro L. G. A. Coutinho. Enhancing dynamic mode decomposition workflow with in situ visualization and data compression. *Engineering with Computers*, March 2023.

Steven L Brunton and J Nathan Kutz. *Data-driven science and engineering: Machine learning, dynamical systems, and control*. Cambridge University Press, 2019.

Apurba Das, M. Nabi, and Francisco Chinesta. Modeling soft robotic actuators using data-driven model reduction. In *2020 28th Mediterranean Conference on Control and Automation (MED)*, pages 490–495, Saint-Raphaël, France, September 2020. IEEE.

Matan Gavish and David L. Donoho. The Optimal Hard Threshold for Singular Values is \(4/\sqrt {3}\). *IEEE Transactions on Information Theory*, 60(8): 5040–5053, August 2014.

Maziar S. Hemati, Matthew O. Williams, and Clarence W. Rowley. Dynamic mode decomposition for large and streaming datasets. *Physics of Fluids*, 26 (11):111701, November 2014.

J Nathan Kutz. *Data-driven modeling & scientific computation: methods for complex systems & big data*. Oxford University Press, 2013.

J Nathan Kutz, Steven L Brunton, Bingni W Brunton, and Joshua L Proctor. *Dynamic mode decomposition: data-driven modeling of complex systems.* SIAM, 2016.

Indranil Nayak, Fernando L. Teixeira, and Robert J. Burkholder. On-the-Fly Dynamic Mode Decomposition for Rapid Time-Extrapolation and Analysis of Cavity Resonances. *IEEE Transactions on Antennas and Propagation*, pages 1–1, 2023.

Zhen Peng, Jun Li, and Hong Hao. Data driven structural damage assessment using phase space embedding and Koopman operator under stochastic excitations. *Engineering Structures*, 255:113906, March 2022.

Clarence W. Rowley, Igor Mezić, Shervin Bagheri, Philipp Schlatter, and Dan S. Henningson. Spectral analysis of nonlinear flows. *Journal of Fluid Mechanics*, 641:115–127, December 2009.

Akira Saito and Tomohiro Kuno. Data-driven experimental modal analysis by Dynamic Mode Decomposition. *Journal of Sound and Vibration*, 481:115434, September 2020.

P. J. Schmid, L. Li, M. P. Juniper, and O. Pust. Applications of the dynamic mode decomposition. *Theoretical and Computational Fluid Dynamics*, 25(1-4):249–259, June 2011.

Peter J. Schmid. Dynamic mode decomposition of numerical and experimental data. *Journal of Fluid Mechanics*, 656:5–28, August 2010.

Peter J Schmid. Dynamic mode decomposition and its variants. *Annual Review of Fluid Mechanics*, 54:225–254, 2022. Publisher: Annual Reviews.

C Hari Manoj Simha and Mohammad Biglarbegian. A note on the use of Dynamic Mode Decomposition in mechanics. *Mechanics Research Communications*, 120:103848, 2022. Publisher: Pergamon.

Ralph C Smith. *Uncertainty quantification: theory, implementation, and applications*, volume 12. Society for Industrial and Applied Mathematics, 2013.

Jonathan H. Tu, Clarence W. Rowley, Dirk M. Luchtenburg, Steven L. Brunton, and J. Nathan Kutz. On dynamic mode decomposition: Theory and applications. *Journal of Computational Dynamics*, 1(2):391–421, 2014.

D. Z. Turner. Digital Image Correlation Engine (DICe) Reference Manual. Technical Report SAND2015-10606 O, Sandia National Laboratories, 2015.